Electronic Supplementary Material (ESI) for Energy & Environmental Science.

*Supplementary Information*

# Efficient Solar Energy Conversion via Bionic Sunlight-driven Ion Transport Boosted by Synergistic Photo-electric/thermal Effects

Jin Wang, * Di Wang, Zeyuan Song, Na Jiang, Shangzhen Li, Yufei Zhang,* Bo Huang, Huijiao Zhou, Zheng Cui, and Lei Wang*

*E-mail: wangjin@xauat.edu.cn, zhangyufei@xauat.edu.cn, wl0178@126.com

**Table of Contents**

## 1. Experimental Section

### Materials and Methods

The phase structure of $Ti_3C_2T_x$ and g-$C_3N_4$/CTS membrane were obtained through X-ray diffraction (XRD, UltimqlV, Japan) using Cu Kα radiation from 10° to 60° with a step of 0.02°. Microstructures and elemental distribution analysis of $Ti_3C_2T_x$, *g*-$C_3N_4$/CTS membrane and nanosheets were achieved through a scanning electron microscope (SEM, Zeiss Gemini SEM 300, Germany). The $Ti_3C_2T_x$, *g*-$C_3N_4$/CTS nanosheets and membranes surface images were captured via the atomic force microscopy (AFM, Bruker Multimode 8) under tapping mode. The morphology of the nanosheets was characterized by transmission electron microscopy (TEM Talos F200X, USA). The UV-vis and DRS measurements of the $Ti_3C_2T_x$ and *g*-$C_3N_4$/CTS colloidal solutions were performed with an ultraviolet spectrophotometer (UV-3600, Japan). The chemistry property of $Ti_3C_2T_x$ and *g*-$C_3N_4$/CTS were characterized through X-ray photoelectron spectroscopy (XPS) using a Thermo Scientific ESCALAB $Xi^+$ instrument with monochromated Al-Kα radiation. All the binding energies were referenced to the C 1s peak at 284.8 eV. The FTIR spectra were recorded using a Bruker VERTEX 33 unit. The zeta potential measurements were measured by dynamic light-scattering analysis using Zetasizer Nano ZS 90. The photothermal performance of $Ti_3C_2T_x$ and *g*-$C_3N_4$/CTS membranes was monitored by using an IR camera (HIKMICRO, China). The steady-state PL emission spectra (FLS1000, UK) was measured at room temperature to evaluate its electron and hole separation performance. The photoelectrochemical properties of the samples were examined by an electrochemical workstation (DH70000, Donghua, China) using a standard threeelectrode cell. The ion concentration was determined by an inductively coupled plasma optical emission spectrometer (Focused Photonics, ICP-5000, China).

## Synthesis of the $Ti_3C_2T_x$ nanosheets

The $Ti_3C_2T_x$ monolayer nanosheets were synthesized via selectively etching Al in the $Ti_3AlC_2$ powder according to the MILD method. Firstly, 1 g $Ti_3AlC_2$ powder with 1.6 g LiF and 20 mL 9 M HCl aqueous solution at 45℃ for 24 h. Subsequently, the mixture product was washed with deionized water via centrifugation at 3500 rpm until the pH reached 5. The separate sediments were redispersed by deionized water and delaminated by strong manual shaking. Finally, a colloidal solution of $Ti_3C_2T_x$ nanosheets was collected after the suspension was centrifuged at 4000 rpm for 1h.

## Synthesis of the *g*-$C_3N_4$/CTS nanosheets

The melamine powder was first heated at 550℃ for 4 hours to complete the thermal polymerization reaction, yellow bulk *g*-$C_3N_4$ was collected after naturally cooling down to room temperature[1, 2]. To obtain the monolayer *g*-$C_3N_4$ nanosheets, 0.8 g ground *g*-$C_3N_4$ powder was added to 400mL of isopropanol and bath-sonicated for 24 h. After that, the dispersion was vacuum filtered on the Nylon substrate membrane, and the powder was re-dispersed in deionized water. The supernatant contained *g*-$C_3N_4$ nanosheets was collected after high-speed centrifugation. In the surface modification process, 68 μL chitosan solution (10 $mg \cdot L^{-1}$) was added to the *g*-$C_3N_4$ nanosheet dispersion (0.03 $mg \cdot mL^{-1}$) and the mixture was continuously stirred at 500 rpm for 4 hours, ensuring the chitosan molecules were grafted onto the surface of the *g*-$C_3N_4$

nanosheets.

## Fabrication of TCC Membranes

The $Ti_3C_2T_x$ membranes were fabricated by vacuum filtration of the diluted nanosheets aqueous suspension ($0.01\ mg\cdot mL^{-1}$) on the PVDF substrates with 0.22 μm pore size. After drying in the vacuum oven, the freestanding $Ti_3C_2T_x$ membranes with a uniform ordered layered architecture were peeled off the PVDF membrane. The $Ti_3C_2T_x$ membrane thickness was controlled by varying the volume of the $Ti_3C_2T_x$ suspension for filtration. The *g*-$C_3N_4$/CTS membranes were fabricated using the same method. The heterogeneous TCC multilayer membranes were fabricated via a two-step vacuum filtration of $Ti_3C_2T_x$ and *g*-$C_3N_4$/CTS nanosheets. Firstly, after depositing the $Ti_3C_2T_x$ aqueous dispersion onto a PVDF substrate, the filtration process continued until the $Ti_3C_2T_x$ membrane was completely dry. The *g*-$C_3N_4$/CTS nanosheets dispersion was then poured onto the $Ti_3C_2T_x$ membrane to construct the heterogeneous structure.

## Ionic photocurrent measurement

The TCC membrane was mounted in a two-compartment set-up and the light could illuminate onto one side of the membrane through a glass-sealed window. The KCl solutions with the same volume were filled into two reservoirs. In our study, a Xenon lamp (Perfect light Technology, CHF300W) was used as the light source. The light intensity of $200\ mW\cdot cm^{-2}$. Ionic current recordings were recorded with a Keithley 2450 source meter through Ag/AgCl electrodes. To avoid unnecessary light contamination, the electrodes were protected and kept away from the membrane.

## Simulation of temperature-responsive ion transport

The theory investigation of ion transport behavior in the nanochannels under the temperature field, the numerical simulation was conducted based on the continuum PNP and Einstein-Stokes theory as follows:

$$\nabla^2\Phi = -\frac{\rho}{\varepsilon} - \frac{F}{\varepsilon}\sum z_i c_i \tag{3}$$

$$j_i = -D_i\left(\nabla c_i + \frac{z_i F c_i}{RT}\nabla\Phi\right) \tag{4}$$

$$\nabla \cdot j_i = 0 \tag{5}$$

$$D_i = \frac{k_B T}{6\pi\eta r} \tag{6}$$

Here, the physical quality $\Phi$ is the electrical potential, $\rho$ is the space charge density, i is the ion species, $z_i$, $c_i$ are the valence and the concentration of species i, $\mathbf{j}_i$ is the local ionic flux, and $D_i$ is the diffusion coefficient. The diffusivity coefficients for cations and anions are $1.957\times10^{-9}$ $m^2/s$ and $2.032\times10^{-9}$ $m^2/s$ (KCl electrolyte is used for simplicity). $T$, $F$, $R$, $k_B$ and $\varepsilon$ represent absolute temperature, Faraday constant, gas constant, Boltzmann constant and dielectric constant of water. The dielectric constant is set to 80.

## DFT theoretical calculation for electron migration

The theoretical calculations in our study were performed with the DFT provided by the program CASTEP package[3,4], which employed the plane-wave basis sets to treat valence electrons and norm-conserving pseudo-potentials to approximate the potential field. The models of the $Ti_3C_2T_x$-*g*-$C_3N_4$ and $Ti_3C_2T_x$-*g*-$C_3N_4$/CTS were built (Figure S35). The exchange-correlation functional was implemented by using the Perdew–Burke–Ernzerhof (PBE)[5] to describe the exchange-correlation energy and electron interactions. The Brillouin zones were separately sampled at 2×2×4, 2×2×4 and 2×2×3 Monkhorst–Pack k-points for the two models[6, 7]. A plane-wave cutoff of 400 eV was used for all calculations. The energy and residual force convergence criterion were set to 2.0 $e^{-6}$ $eV\cdot atom^{-1}$ and 0.05 $eV\cdot Å^{-1}$ for geometry optimization, respectively. A 2×2×4 and 2×2×3 mesh was used to calculate their total density of states (TDOS) and partial density of states (PDOS) for the $Ti_3C_2T_x$-*g*-$C_3N_4$ and $Ti_3C_2T_x$-*g*-$C_3N_4$/CTS. Charge transfer was calculated by electron density difference (EDD) on the basis of the Milliken Population Analysis (MPA)[8].

## 2. Supplement figures

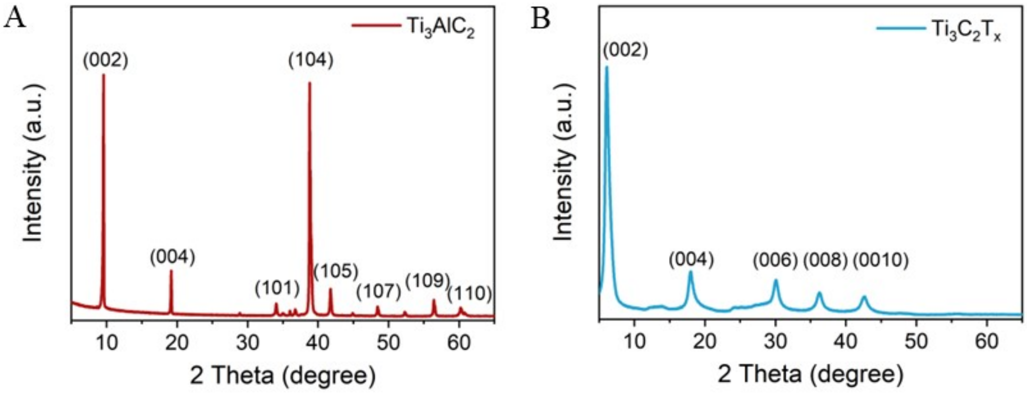

**Figure S1.** (008) diffractive peak at 39° and the left shift of the (002) peak in the XRD spectrum of the $Ti_3C_2T_x$ indicated that the Al layers were successfully etched.

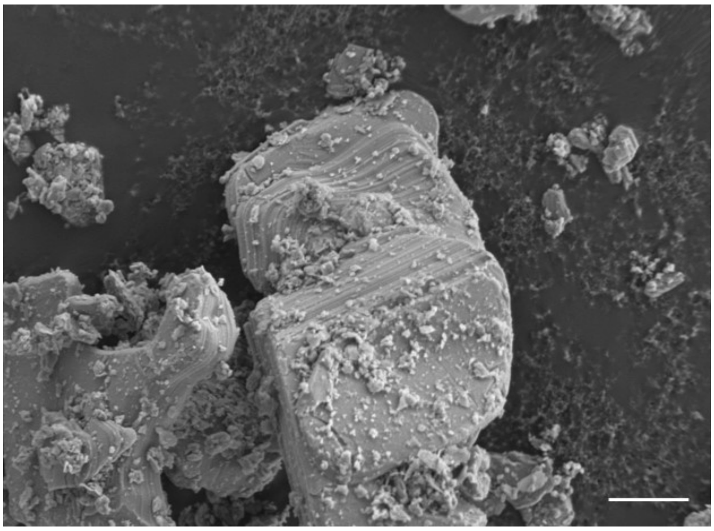

**Figure S2. SEM image of $Ti_3AlC_2$**. Scale bar, 3 μm.

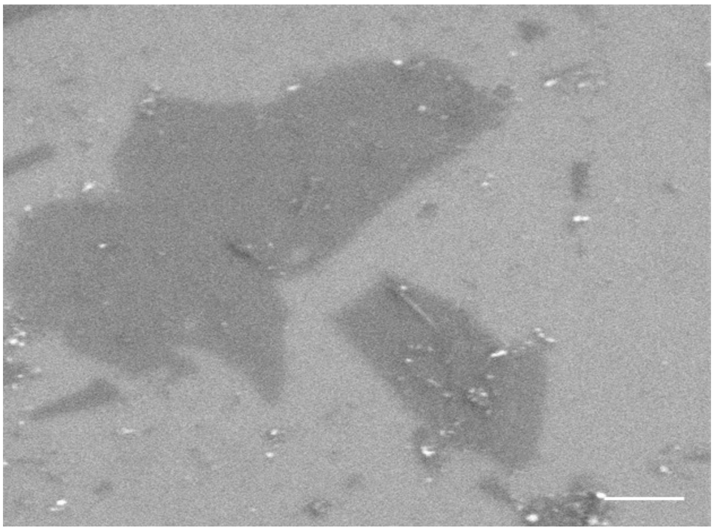

**Figure S3. SEM image of $Ti_3C_2T_x$ nanosheets.** Scale bar, 1 μm.

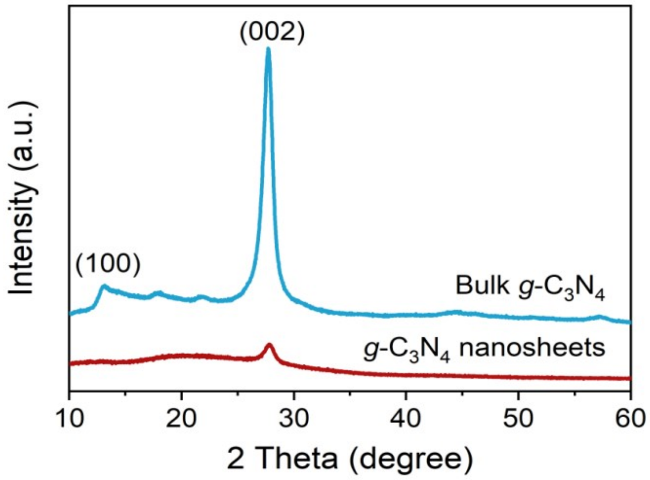

**Figure S4. XRD patterns of Bulk *g*-$C_3N_4$ and *g*-$C_3N_4$ nanosheets.** Compared with Bulk *g*-$C_3N_4$, the intensity of this (002) peak was significantly decreased and the (100) weak peak disappeared.

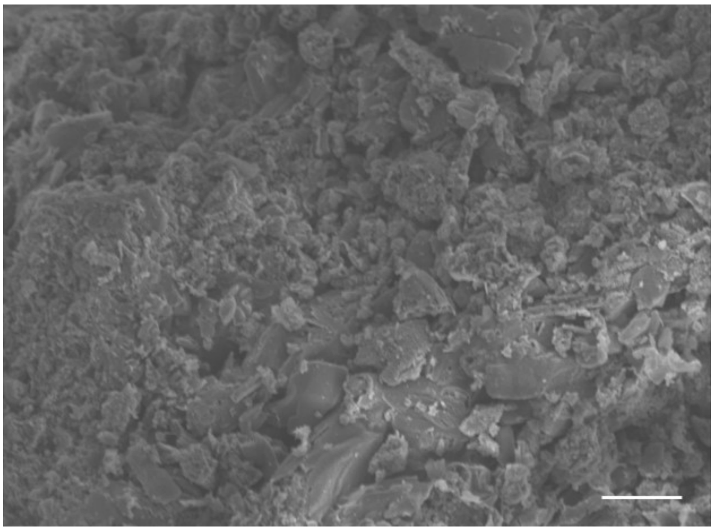

**Figure S5. SEM image of bulk *g*-$C_3N_4$**. Scale bar, 5 μm.

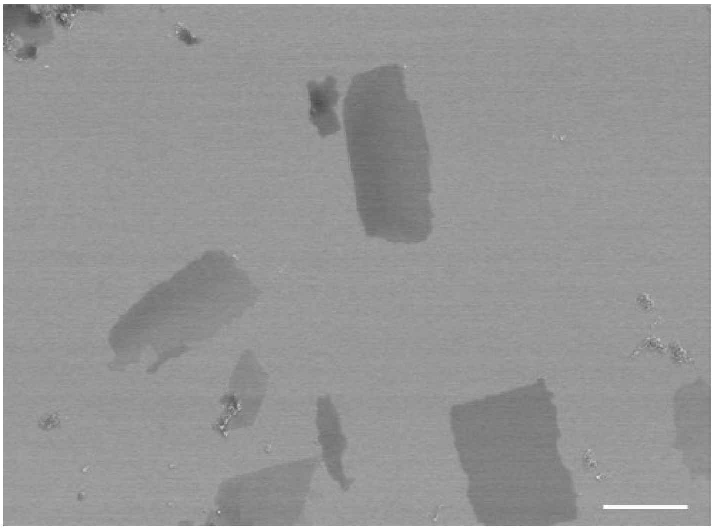

**Figure S6. SEM images of *g*-$C_3N_4$ nanosheets.** Scale bar, 10 μm.

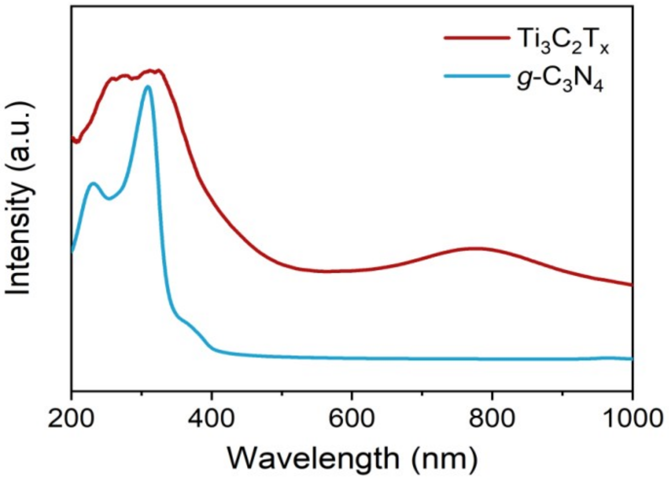

**Figure S7.** UV-vis spectra of the $Ti_3C_2T_x$ and $g$-$C_3N_4$ dispersions.

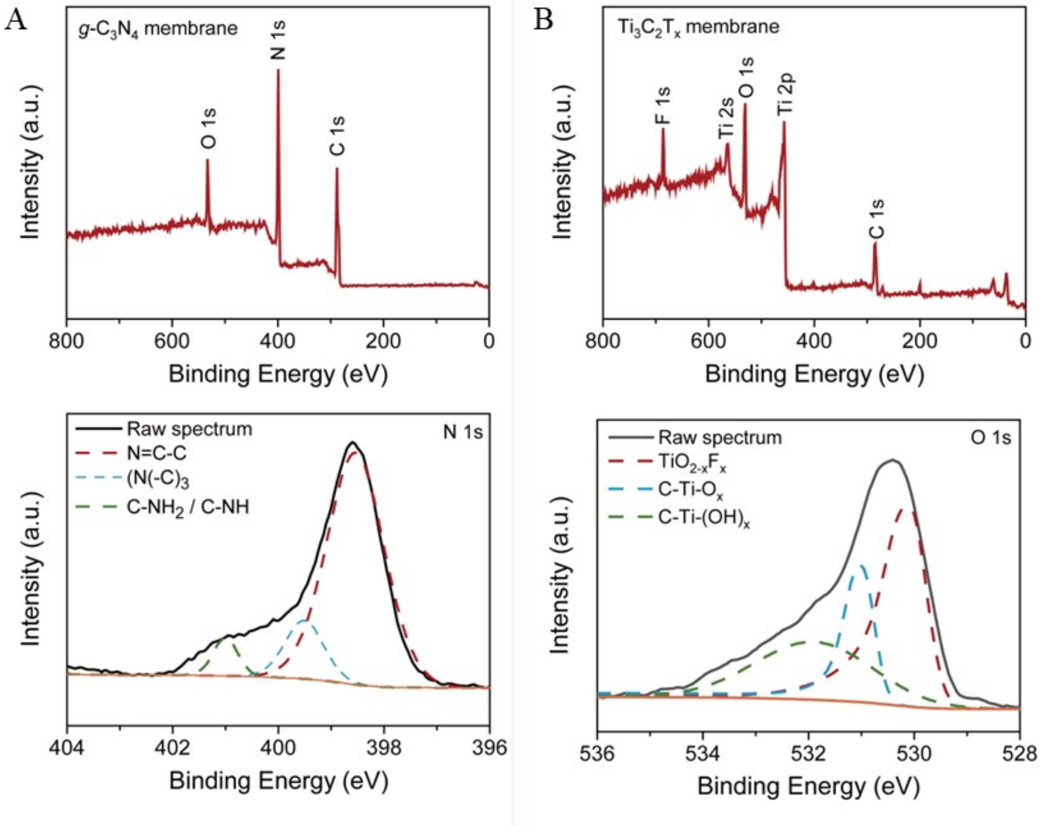

**Figure S8. XPS spectra of the *g*-$C_3N_4$ and $Ti_3C_2T_x$ membrane.** (**A**) XPS results and N 1s region of the *g*-$C_3N_4$ membrane. (**B**) XPS results and O 1s region of the $Ti_3C_2T_x$ membrane.

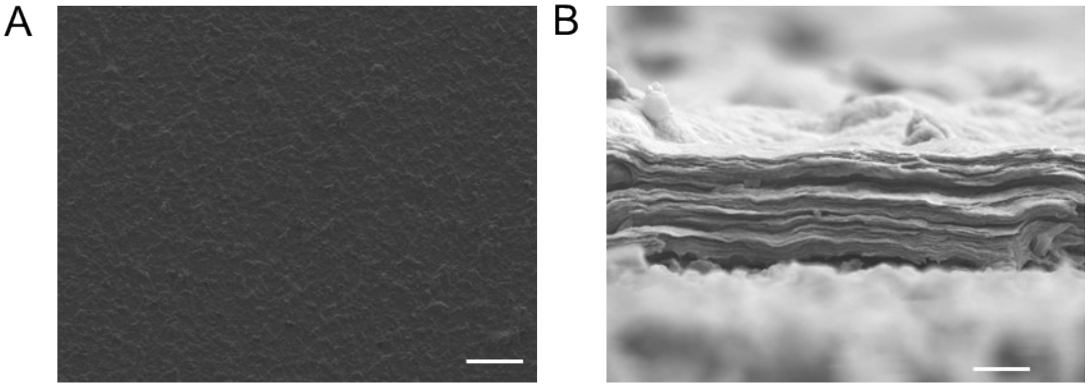

**Figure S9. SEM analysis of the $Ti_3C_2T_x$ membrane.** (**A**) SEM image of the $Ti_3C_2T_x$ membrane surface. Scale bar: 10 µm. (**B**) SEM image of the $Ti_3C_2T_x$ membrane cross-section. Scale bar, 2 µm.

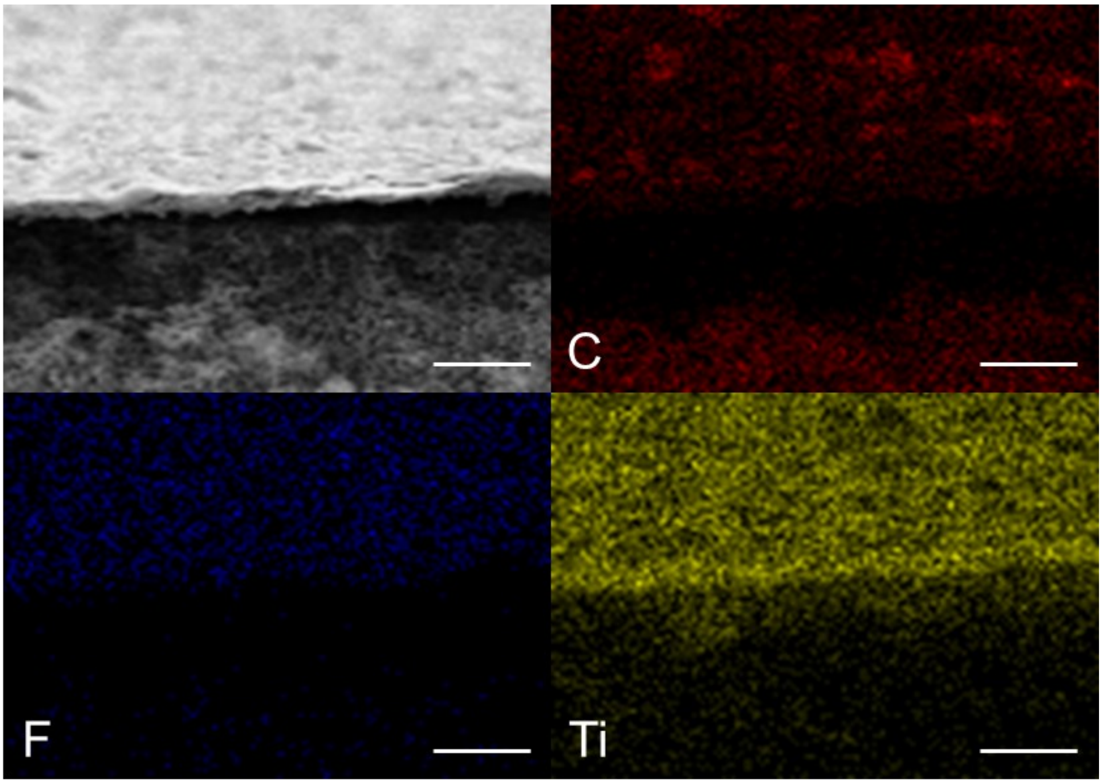

**Figure S10. SEM image of the $Ti_3C_2T_x$ membrane cross-section and elemental mapping.** Scale bar, 10 μm.

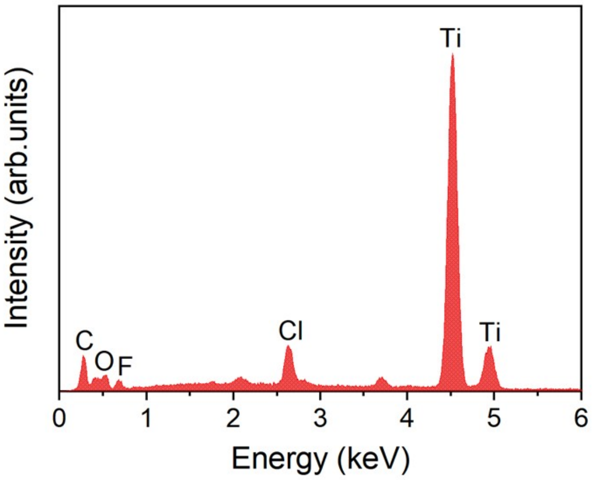

**Figure S11. EDS spectrum of the $Ti_3C_2T_x$ membrane.**

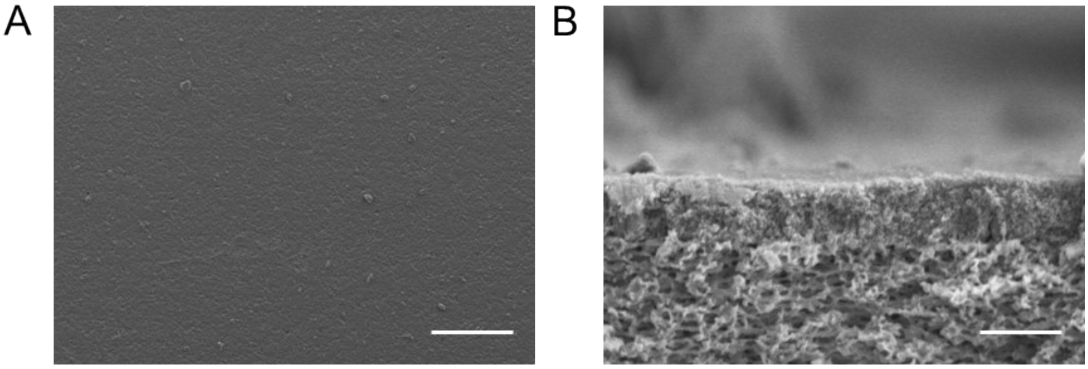

**Figure S12. SEM analysis of the *g*-$C_3N_4$/CTS membrane.** (**A**) SEM image of the *g*-$C_3N_4$/CTS membrane surface. Scale bar: 100 μm. (**B**) SEM image of the *g*-$C_3N_4$/CTS membrane cross-section. Scale bar, 3 μm.

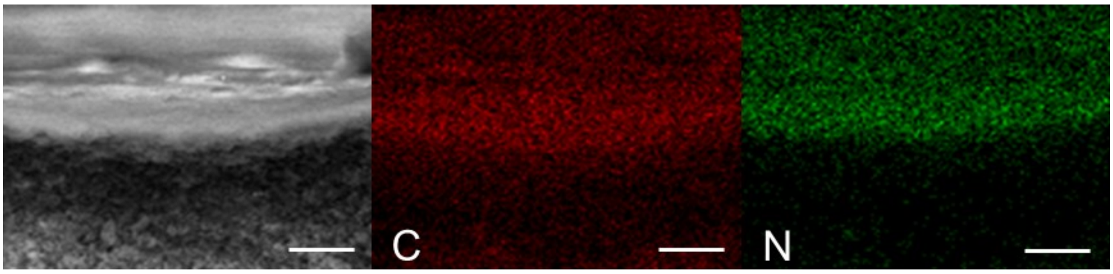

**Figure S13. SEM image of the *g*-$C_3N_4$/CTS membrane cross-section and elemental mapping.** Scale bar, 5 μm.

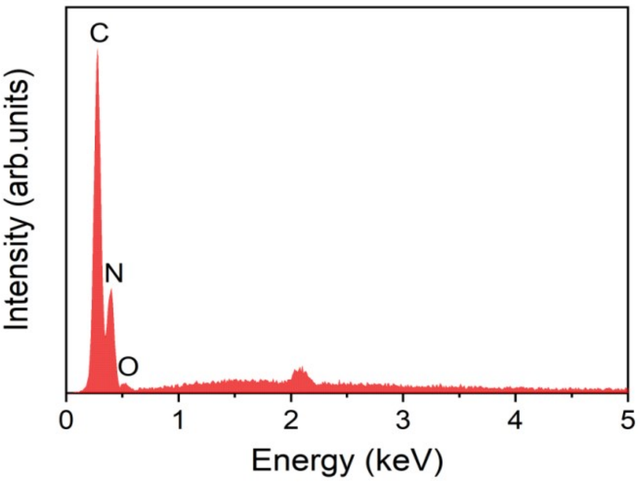

**Figure S14. EDS spectrum of the *g*-$C_3N_4$/CTS membrane.**

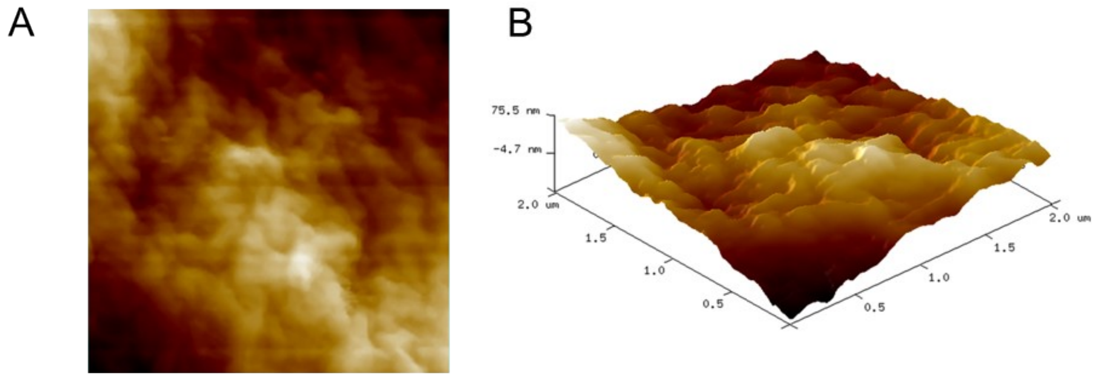

| | **$Ti_3C_2T_x$ membrane** |
|---|---|
| **Rq (nm)** | 21.4 |
| **Ra (nm)** | 16.7 |

**Figure S15. AFM images of the $Ti_3C_2T_x$ membrane surface with a scan area of 2 µm × 2 µm.** (**A**) 2D and (**B**) 3D AFM images. The table below shows the surface roughness parameters of the $Ti_3C_2T_x$ membrane. Scale bar, 500 nm.

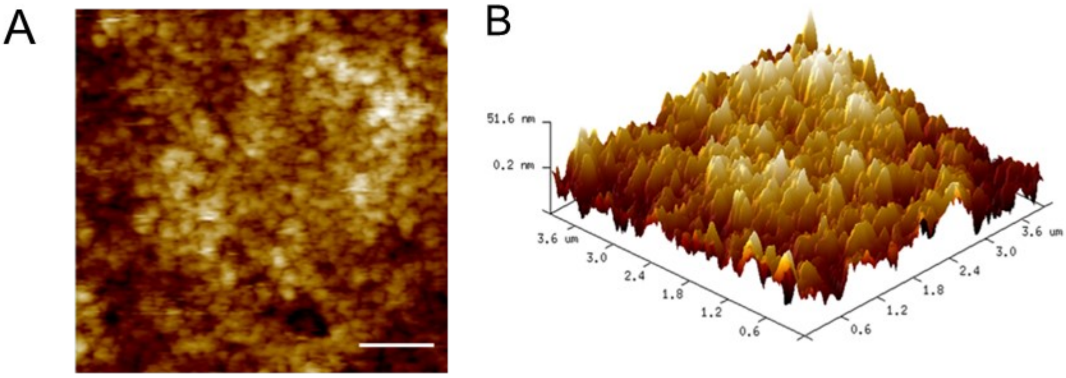

| | **g-$C_3N_4$/CTS membrane** |
|---|---|
| **Rq (nm)** | 14 |
| **Ra (nm)** | 11.2 |

**Figure S16. AFM images of the *g*-$C_3N_4$/CTS membrane surface with a scan area of 3.6 µm × 3.6 µm.** (**A**) 2D and (**B**) 3D AFM images. The table below shows the surface roughness parameters of the *g*-$C_3N_4$/CTS membrane. Scale bar, 600 nm.

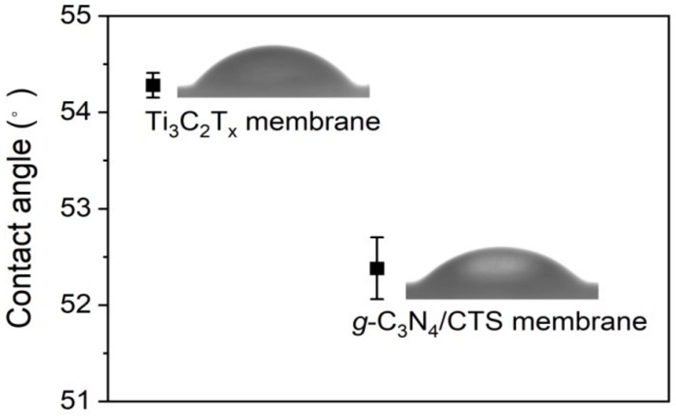

**Figure S17. Contact angle of water on the $Ti_3C_2T_x$ and *g*-$C_3N_4$/CTS membrane surfaces.** The error bars represent the standard deviations.

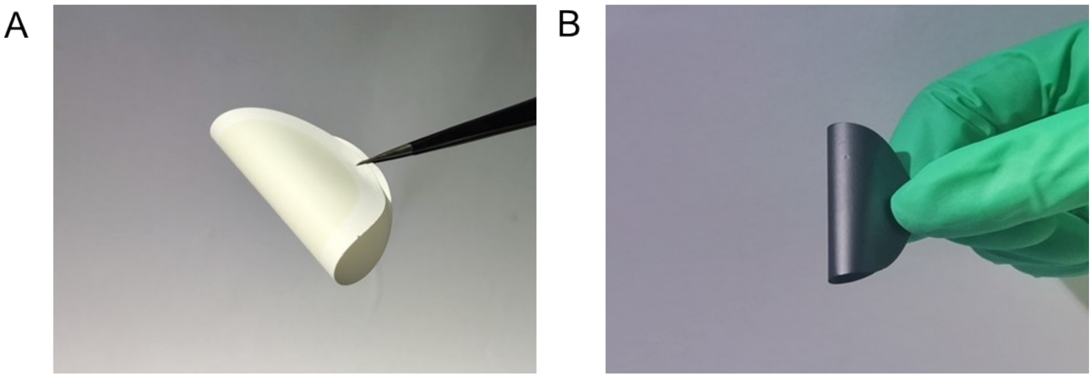

**Figure S18. Optical images of (A) *g*-$C_3N_4$/CTS and (B) $Ti_3C_2T_x$ membrane.**

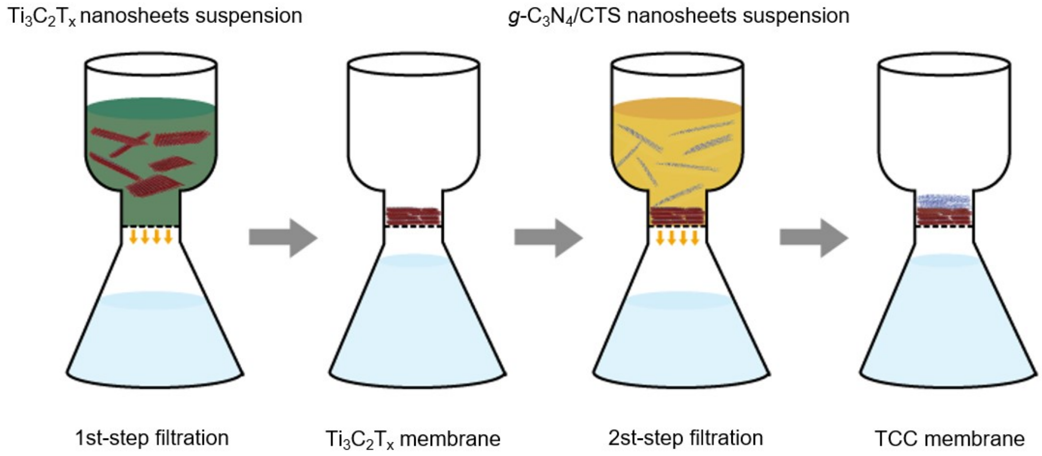

**Figure S19. Scheme of the fabrication of TCC membrane.**

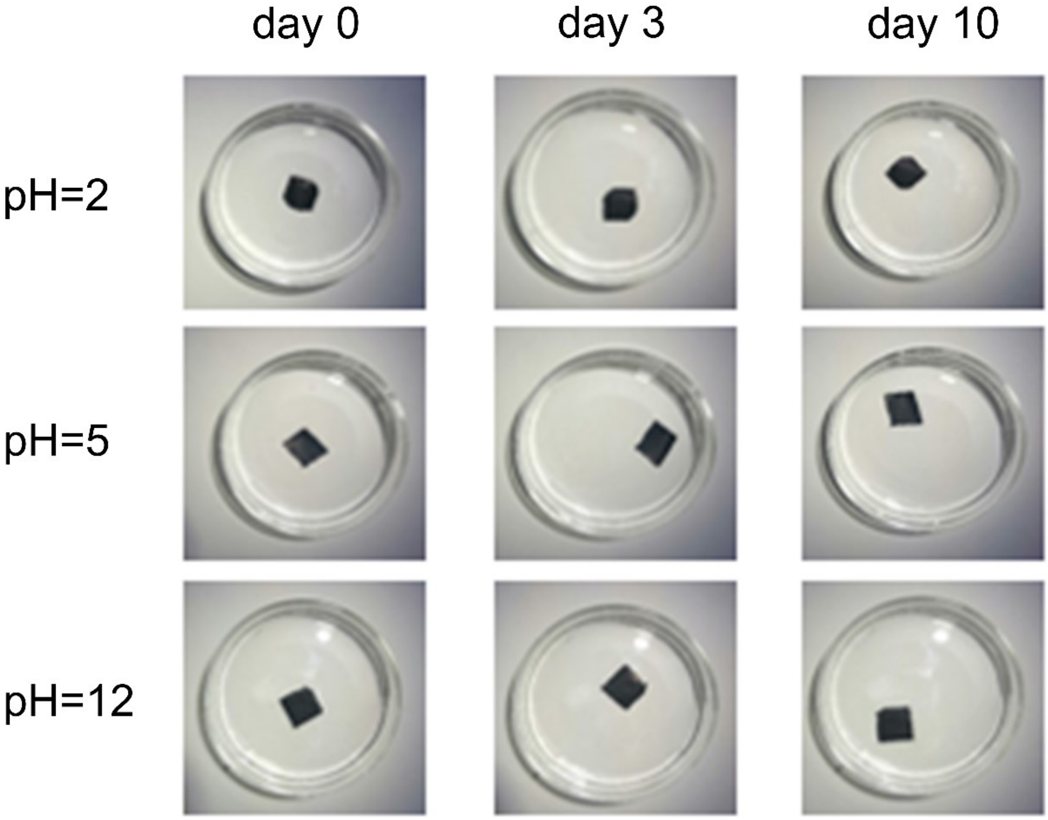

**Figure S20. Stability of TCC membrane.** Photos of the TCC membrane samples soaked in aqueous solution of pH 2, 5, and 12. The soaking time was 3 and 10 days.

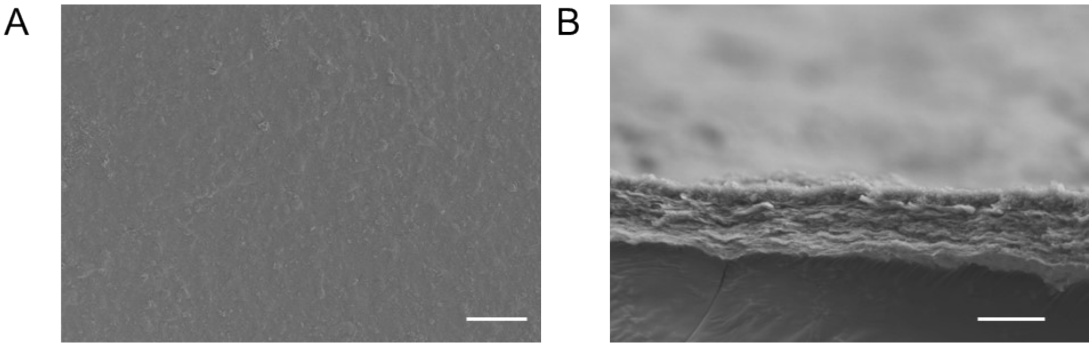

**Figure S21. SEM analysis of the TCC membrane.** (**A**) SEM image of the TCC membrane surface. Scale bar, 20 μm. (**B**) SEM image of the TCC membrane cross-section. Scale bar, 2 μm.

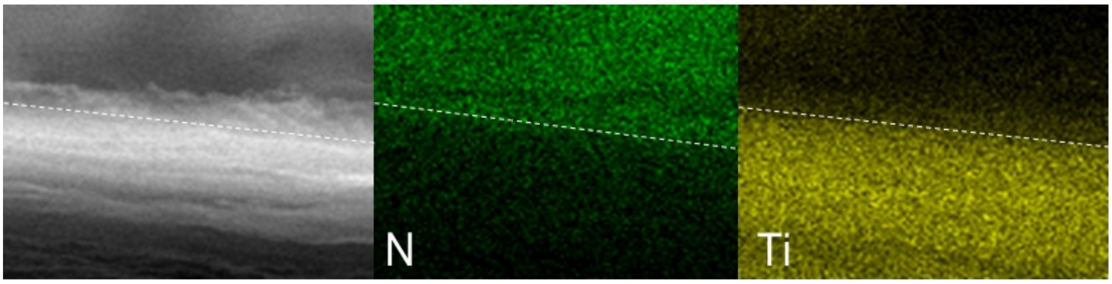

**Figure S22. SEM image of the TCC membrane cross-section and elemental mapping.** Scale bar, 1 μm.

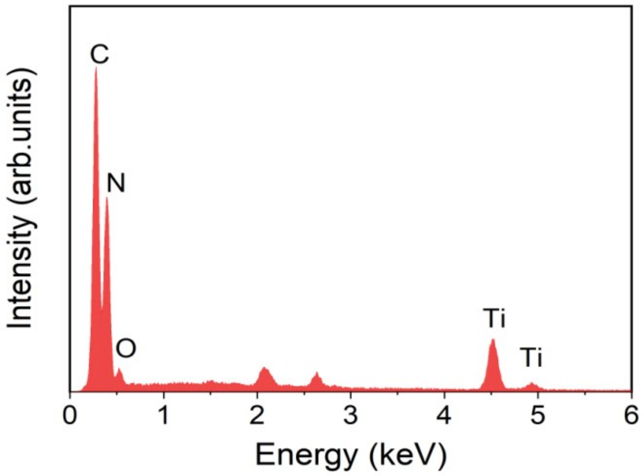

**Figure S23. EDS spectrum of the TCC membrane.**

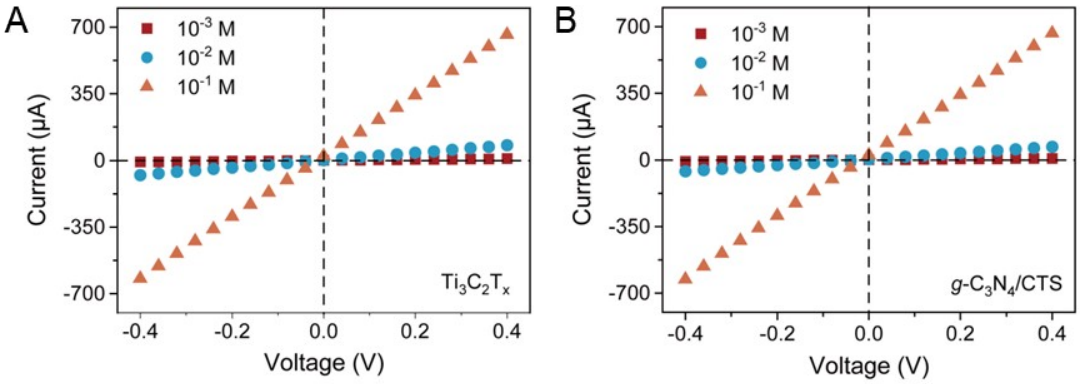

**Figure S24. Current-voltage curves of the $Ti_3C_2T_x$ and *g*-$C_3N_4$/CTS membrane.**

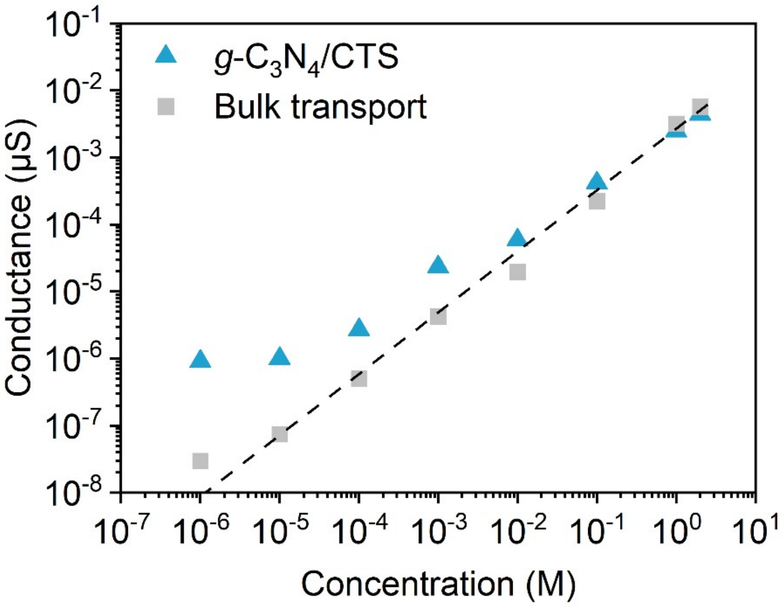

**Figure S25. Ionic conductance of bulk solutions and *g*-$C_3N_4$/CTS membrane versus salt concentration (thickness: 1.5 µm).** It was difficult to detach the *g*-$C_3N_4$/CTS membrane from the PVDF substrate, therefore the test was conducted using the composite membrane.

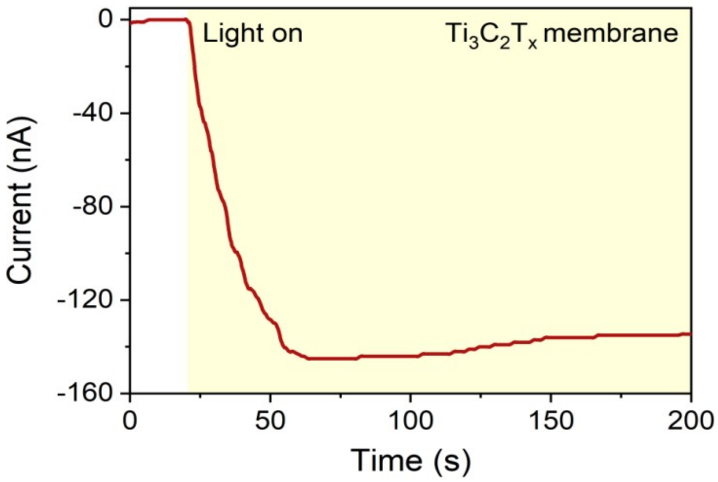

**Figure S26.** **Long-term ionic current in $Ti_3C_2T_x$ membrane.**

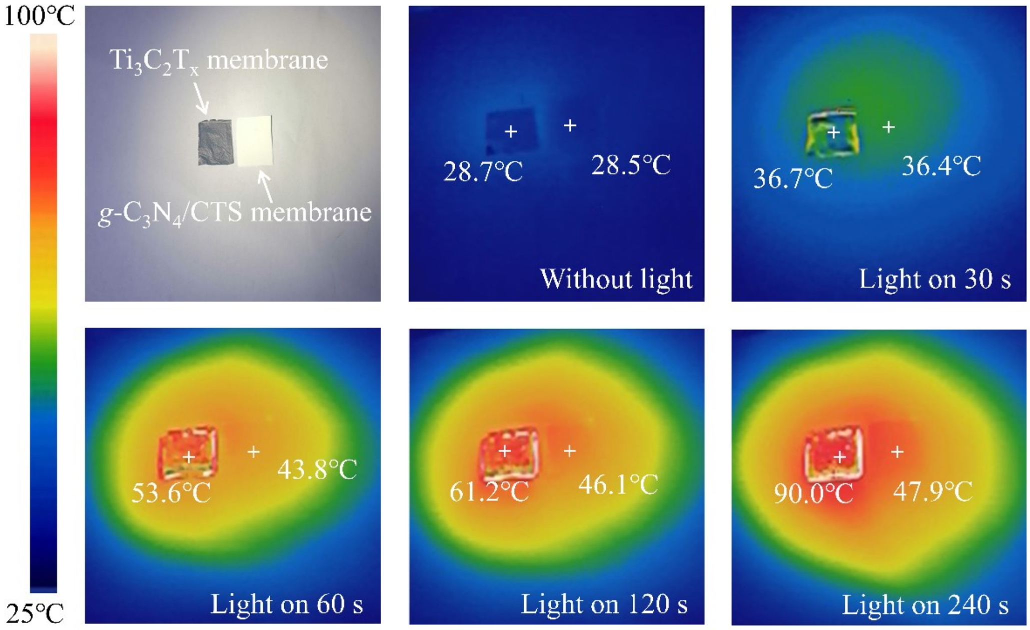

**Figure S27. Light-to-heat conversion phenomenon.** IR thermal images of $Ti_3C_2T_x$ and *g*-$C_3N_4$/CTS membrane under light irradiation taken at different time intervals.

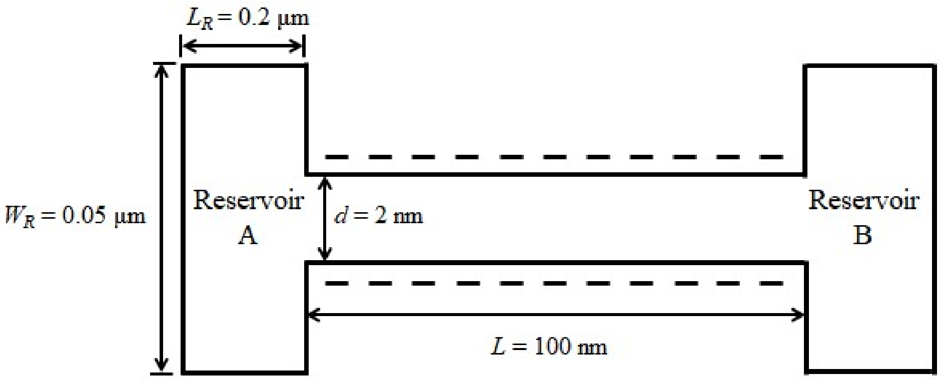

**Figure S28. Scheme of the simulation model channel.** Two reservoirs ($L_R$ =0.2 μm, $W_R$ =0.05 μm) were connected by a charged channel ($d$ = 2 nm and $L$ = 100 nm). The surface charge density in nanochannel was -15 mC $m^{-2}$. The KCl solutions were set at the value of 0.01 M.

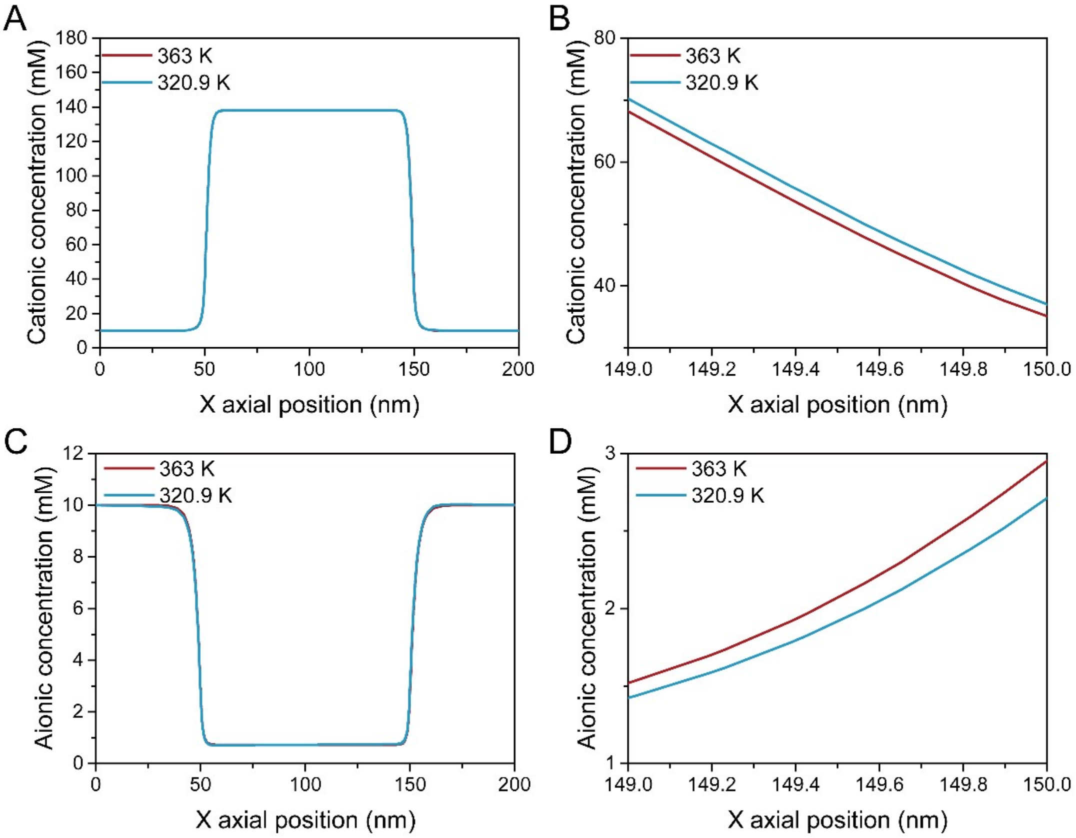

**Figure S29. Scheme of K$^+$ and Cl$^-$ ion concentration profiles before (blue curve) and after (red curve) the temperature change.** The (**B**) and (**D**) images were the magnifications at the orifice of nanochannel/reservoir B corresponding to the (**A**) and (**C**) images, respectively. The temperatures of reservoir A and nanochannel were kept constant at 320.9K, while reservoir B was increased from the initial 320.9K to 363K. It should be noted that the sharp temperature boundary at the nanochannel/reservoir B orifice was set and the heat conduction was not considered here for simplicity.

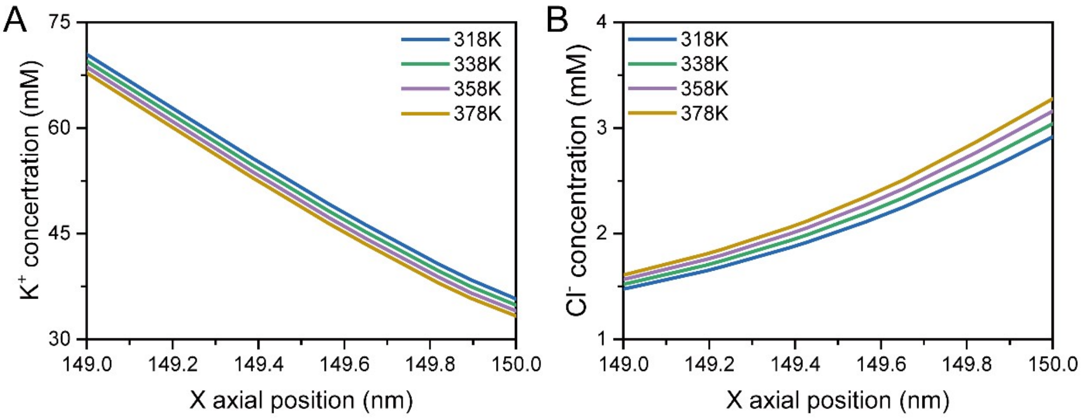

**Figure S30. Changes of cation and anion after temperature continuously increased.**

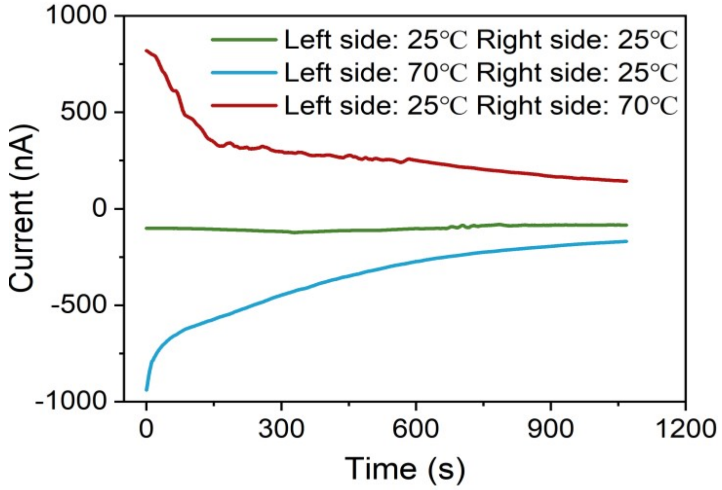

**Figure S31. Photothermal effect simulation.** The electrolyte solution (KCl, 0.01M) added to both reservoirs are with equal concentration. Specifically, a heated KCl solution with a temperature value of approximately 70°C and a room-temperature solution was filled in the two reservoirs, respectively to simulate the photothermal experiment conditions.

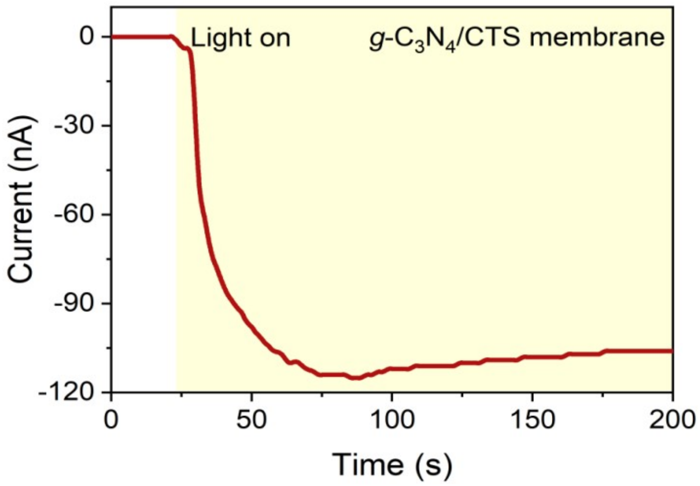

**Figure S32. Long-term ionic current in the *g*-$C_3N_4$/CTS membrane.**

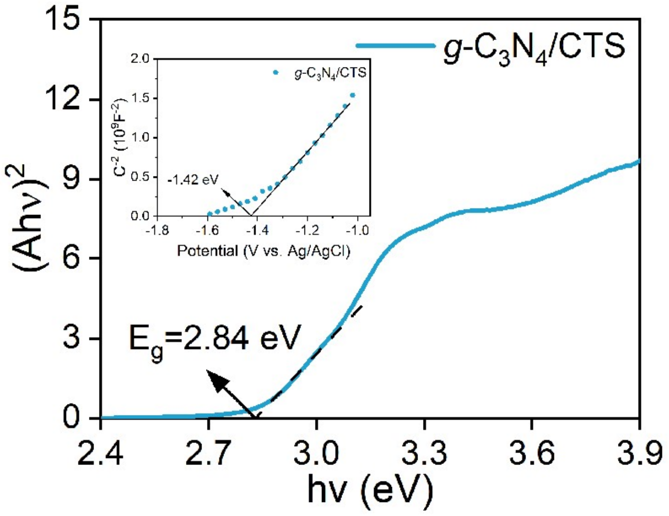

**Figure S33. Corresponding Tauc plots for the *g*-$C_3N_4$/CTS, the inset graph showed Mott-Schottky plots of the *g*-$C_3N_4$/CTS.**

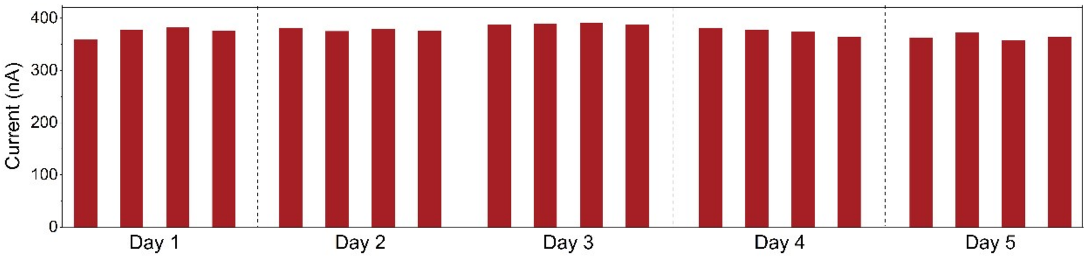

**Figure S34. Daily photo-response tests for long-term stability**

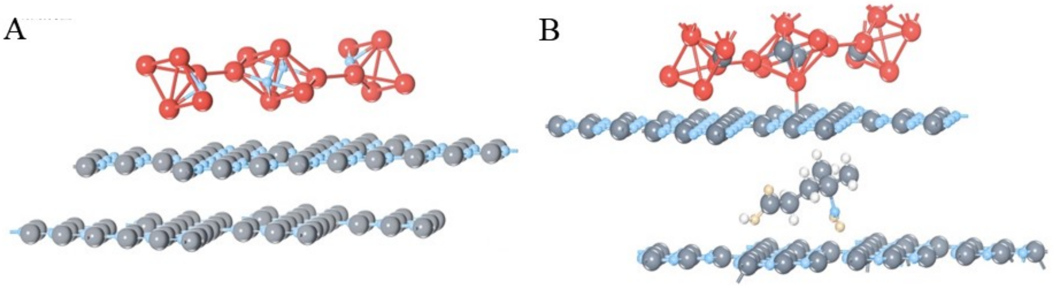

**Figure S35. The models of the $Ti_3C_2T_x$-*g*-$C_3N_4$ (A) and $Ti_3C_2T_x$-*g*-$C_3N_4$/CTS (B) were built.**

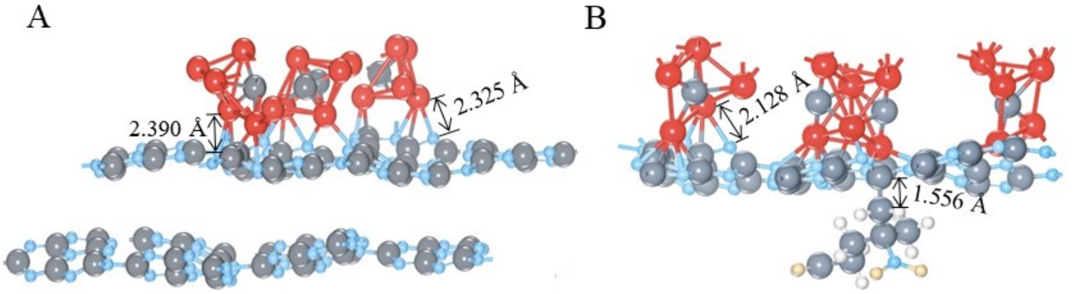

**Figure S36. $Ti_3C_2T_x$-*g*-$C_3N_4$ (A) and $Ti_3C_2T_x$-*g*-$C_3N_4$/CTS (B) crystal model diagrams constructed after geometry optimization.**

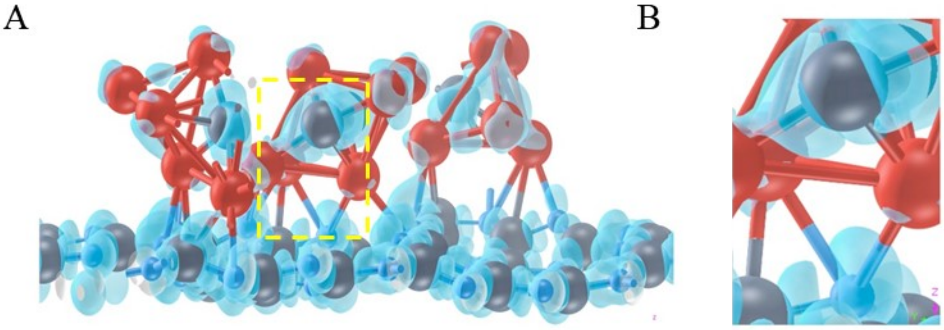

**Figure S37. The Milliken Population Analysis (MPA) plot based on EDD results of $Ti_3C_2T_x$-*g*-$C_3N_4$.**

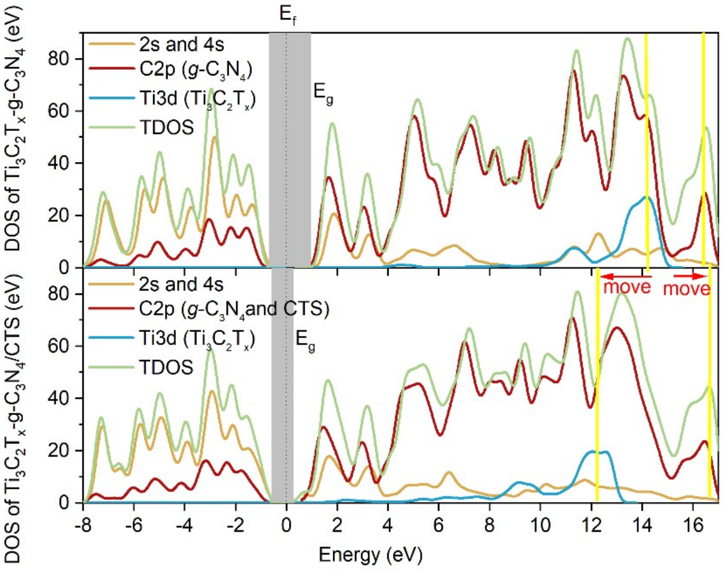

**Figure S38. The electron density of states (DOS) diagram of $Ti_3C_2T_x$-*g*-$C_3N_4$ and $Ti_3C_2T_x$-*g*-$C_3N_4$/CTS**

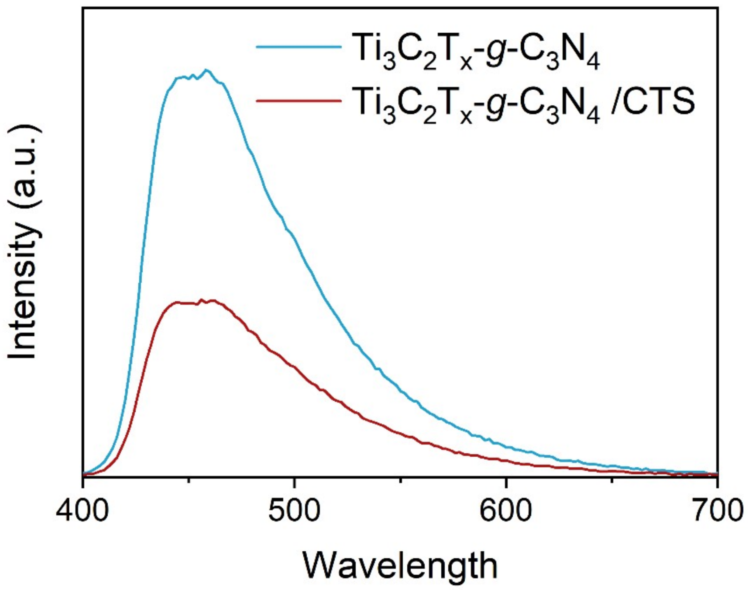

**Figure S39. Steady photoluminescence (PL) spectra of $Ti_3C_2T_x$-*g*-$C_3N_4$ and $Ti_3C_2T_x$-*g*-$C_3N_4$/CTS**

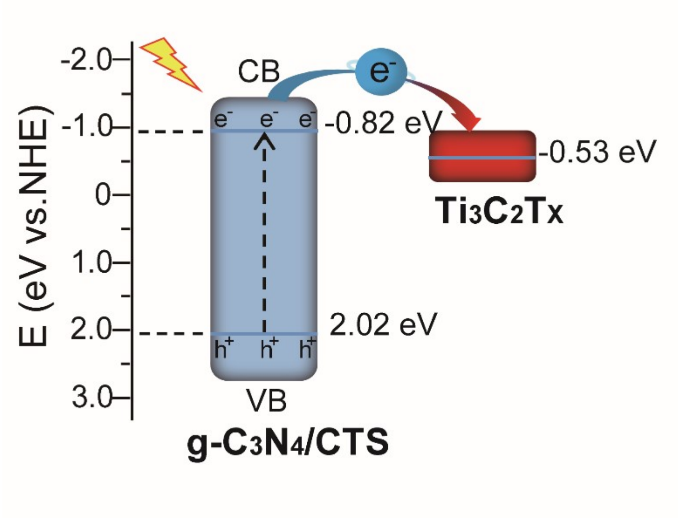

**Figure S40. Schematic illustration of the band structure in the TCC membrane.**

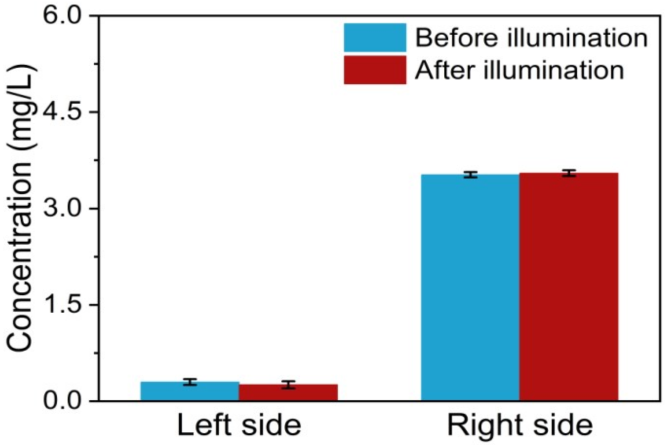

**Figure S41. Concentration of $K^+$ ions measured by inductively coupled plasma (ICP) before and after illumination.**

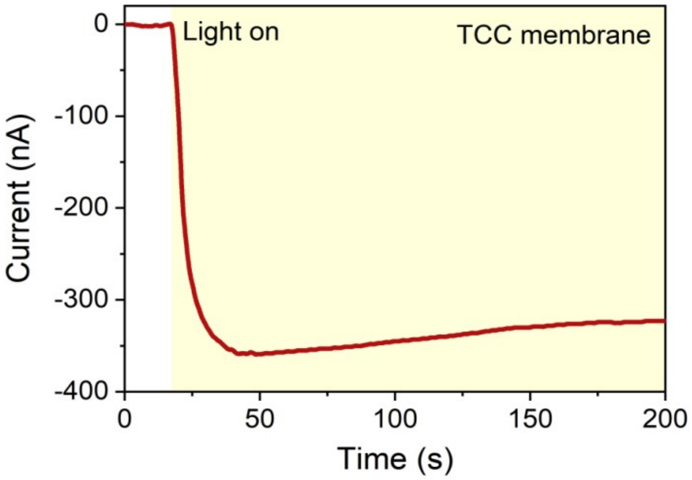

**Figure S42.** Long-term ionic current in the TCC membrane.

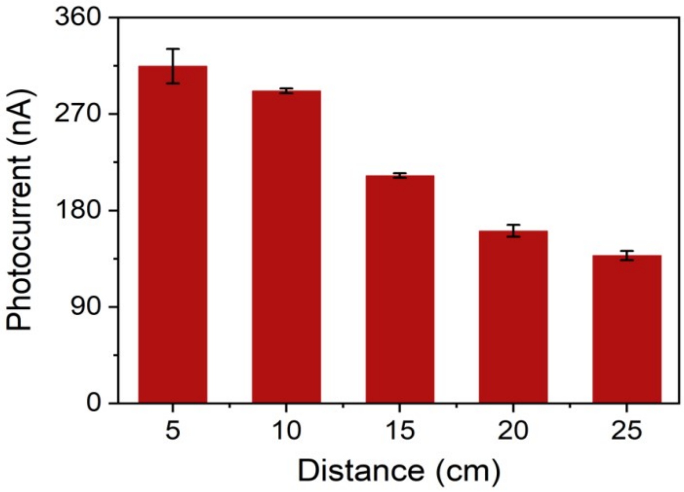

**Figure S43. Light intensity dependence of the photocurrent measured on TCC membrane. The distance between the light source and device was adjusted to investigate the effect of light intensity.** The electrolyte concentrations were 0.01 M KCl. Error bars denote standard deviation.

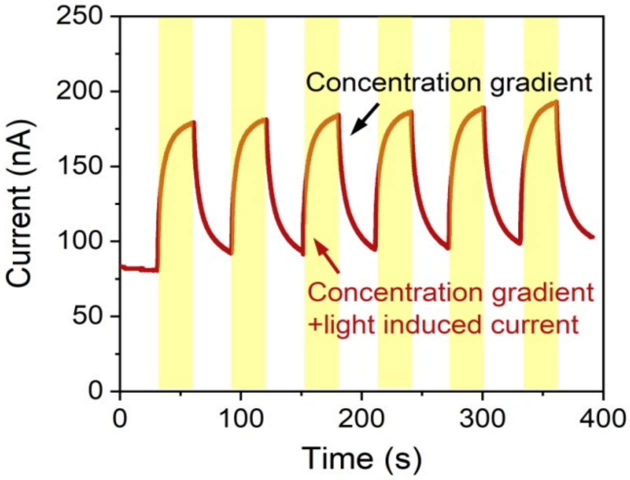

**Figure S44. Measured cyclic constant current with alternating illumination (KCl, $C_L$=10$C_R$=$10^{-4}$ M).**

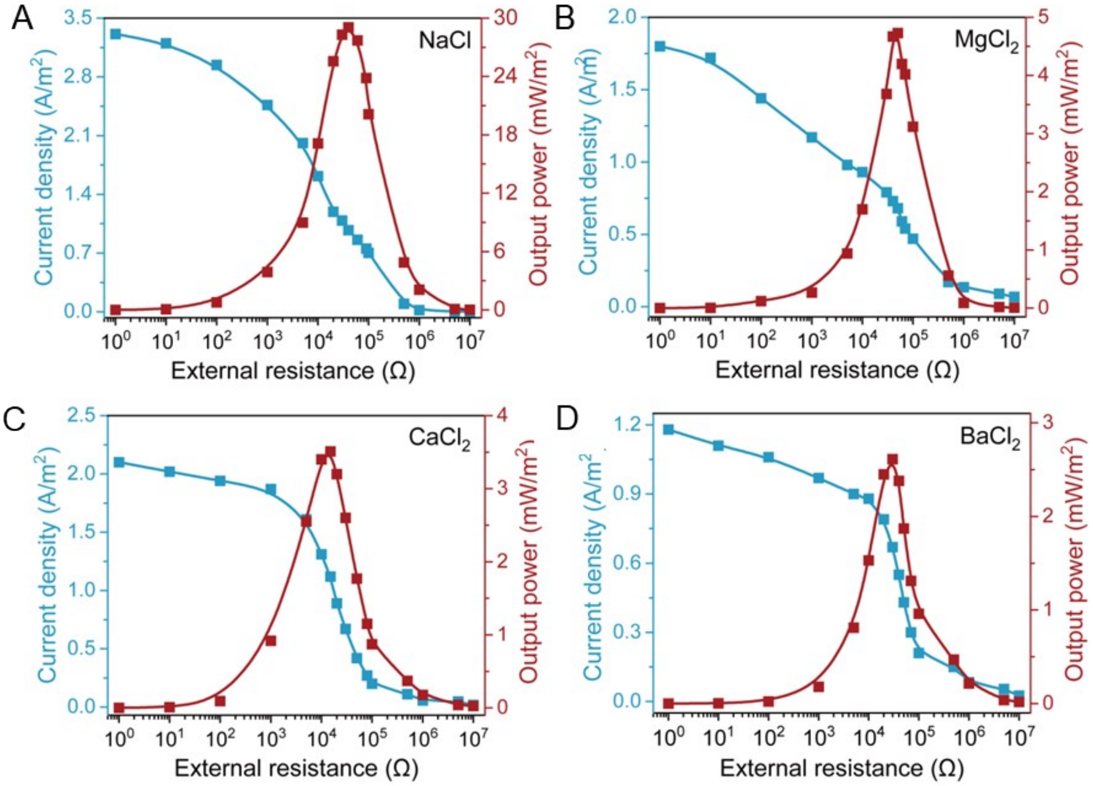

**Figure S45. Light-to-ionic energy conversion performance for different salt solutions containing monovalent or divalent ions.** The electrolyte concentration was set at $10^{-2}$ M.

**Table S1.** Hydration free energy of different ions. [9]

| Ion | Hydration free energy (KJ/mol) |
|---|---|
| **$K^+$** | -321 |
| **$Na^+$** | -405 |
| **$Li^+$** | -515 |
| **$Ca^{2+}$** | -1549 |
| **$Mg^{2+}$** | -1922 |

**Table S2.** Anti-gradient ion transport data comparison.

| Materials | Concentration gradient | Ref. |
|---|---|---|
| **Graphene Oxide membrane** | 10/1 | 10 |
| **Graphene Oxide membrane** | 10/1 | 11 |
| **$Ti_3C_2T_x$ membrane** | 10/1 | 12 |
| **$Ti_3C_2T_x$ membrane** | 5/1 | 13 |
| **Graphene Oxide membrane** | 4/1 | 14 |
| **$Ti_3C_2T_x$-g-$C_3N_4$/chitosan composite membrane** | 20/1 | Our work |

## 3. References

1. X. Zhang, X. Xie, H. Wang, J. Zhang, B. Pan and Y. Xie, *J Am Chem Soc*, 2013, **135**, 18-21.
2. D. Zhao, J. Chen, C.-L. Dong, W. Zhou, Y.-C. Huang, S. S. Mao, L. Guo and S. Shen, *Journal of Catalysis*, 2017, **352**, 491-497.
3. S. Peng, R. Li, Y. Huang, Y. Zhang, J.-j. Cao and S. Lee, *Applied Surface Science*, 2022, **600**, 154056.
4. Y. Zhang, Y. Huang, S. C. Lee and J.-j. Cao, *Chemical Engineering Journal*, 2020, **380**, 122498.
5. J. P. Perdew, K. Burke and M. Ernzerhof, *Physical review letters*, 1996, **77**, 3865.
6. P. E. Blöchl, *Physical review B*, 1994, **50**, 17953.
7. H. J. Monkhorst and J. D. Pack, *Physical review B*, 1976, **13**, 5188.
8. R. S. Mulliken, *The Journal of Chemical Physics*, 1955, **23**, 1833-1840.
9. B. Tansel, *Separation and purification technology*, 2012, 86, 119-126.
10. J. Yang, X. Hu, X. Kong, P. Jia, D. Ji, D. Quan, L. Wang, Q. Wen, D. Lu and J. Wu, *Nature communications*, 2019, **10**, 1-7.
11. Y. Zhang, F. Li, X. Kong, T. Xue, D. Liu, P. Jia, L. Wang, L. Ding, H. Dong and D. Lu, *Advanced Functional Materials*, 2020, **30**, 1907549.
12. R. Li, L. Zhang, L. Shi and P. Wang, *ACS nano*, 2017, **11**, 3752-3759.
13. K. Xiao, L. Chen, R. Chen, T. Heil, S. D. C. Lemus, F. Fan, L. Wen, L. Jiang and M. Antonietti, *Nature communications*, 2019, **10**, 1-7.
14. D. Quan, D. Ji, Q. Wen, L. Du, L. Wang, P. Jia, D. Liu, L. Ding, H. Dong and D. Lu, *Advanced Functional Materials*, 2020, **30**, 2001549.